Nano Research

Open Access

Research Article

Direct photopatterning of perovskite nanocrystal films for building pixelated photodetector arrays

Hannikezi Abudukeremu[1,§], Guan-Hua Dun[2,§], Hengwei Qiu[1], Dan Liu[1], Fu Li[3], Song Wang[1], Junyang Hou[1], Wangyu Liu[1], Mingfeng Cai[1], Tian-Ling Ren[2] ✉, Hao Zhang[1] ✉, and Jinghong Li[1] ✉

[1] *Department of Chemistry, Center for BioAnalytical Chemistry, Key Laboratory of Bioorganic Phosphorus Chemistry & Chemical Biology (Ministry of Education), Tsinghua University, Beijing 100084, China*
[2] *School of Integrated Circuits and Beijing National Research Center for Information Science and Technology (BNRist), Tsinghua University, Beijing 100084, China*
[3] *State Key Laboratory of Transducer Technology, Shanghai Institute of Microsystem and Information Technology, Chinese Academy of Sciences, Shanghai 200050, China*
§ *Hannikezi Abudukeremu and Guan-Hua Dun contributed equally to this work.*

Cite this article: *Nano Research*, **2025**, *18*, 94907279. https://doi.org/10.26599/NR.2025.94907279

ABSTRACT: Metal halide-based perovskites, with their exceptional photoelectric conversion efficiency, are promising materials for photodetectors and image sensors. Achieving high-definition optical imaging requires not only high-quality perovskite materials but also effective patterning methods. Here, we show the fabrication of pixelated photodetector arrays through a two-step process: (1) direct optical patterning of $CsPbBr_3$ perovskite nanocrystal films using ligand cross-linkers, and (2) post-patterning ligand-exchange process. The direct optical patterning achieves high-resolution (≈ 2 μm in pixel sizes), uniform $CsPbBr_3$ nanocrystal film patterns over 2-inch wafers. The ligand-exchange process replaces the long hydrocarbon ligands and cross-linkers with compact ionic ligands, which enhance the charge transport efficacy without compromising the quality of the patterned films. Consequently, the patterned photodetectors, in the photoconductor configuration, show responsivity (0.11 $A \cdot W^{-1}$) and specific detectivity (1.81×10^{11} Jones) on par with their non-patterned counterparts. These features permit the creation of pixelated photodetector arrays that minimize the charge-sharing crosstalk effect and enable improved imaging capabilities. This work shows a promising approach in building high-performance perovskite image sensors.

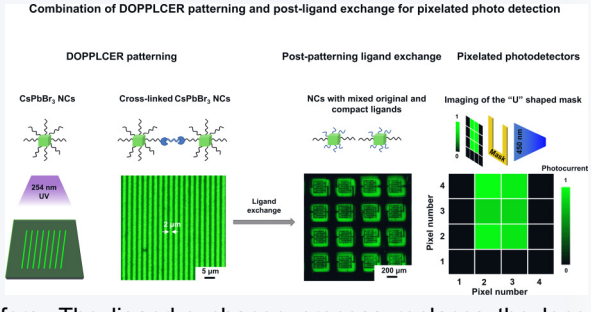

KEYWORDS: perovskite nanocrystals, patterning, photodetectors, image sensors

1 Introduction

Metal halide-based perovskites, characterized by their strong light absorption, tunable bandgap, and facile processability, have emerged as promising active materials in various optoelectronic devices, including photovoltaics [1], light-emitting diodes [2], and photodetectors [3]. Among these device applications, perovskite-based photodetectors possess tunable spectral responses, low operating voltage, and great compatibility with flexible substrates [4], making them highly suitable for image sensing [5], optical communication [6], and health monitoring [7]. Additionally, the large variety of compositions (fully inorganic and organic/inorganic hybrid perovskites) and morphologies/dimensions (e.g., single crystals [8], and three-dimensional (3D) [9], and low-dimensional polycrystalline structures [10]) have endowed perovskites with excellent material versatility and great flexibility in optimizing the device performance [11, 12].

Moving forward to building perovskite-based photodetector arrays and image sensors necessitates the effective and precise patterning of perovskite materials. Achieving this is challenging due to the inherent instability of perovskites when exposed to solvents, irradiation, and other dry/wet etching conditions involved in typical photo- and electron-beam lithographic techniques [13, 14]. During the past years, various patterning strategies have been developed for perovskites in different dimensions. The most widely explored

Received: December 18, 2024; **Revised:** January 26, 2025
Accepted: January 27, 2025

✉Address correspondence to Tian-Ling Ren, RenTL@tsinghua.edu.cn; Hao Zhang, hzhangchem@mail.tsinghua.edu.cn; Jinghong Li, jhli@mail.tsinghua.edu.cn

strategies involve the selective deposition and growth of perovskite single crystals or polycrystalline films on physically or chemically defined substrates [15–19], as well as the guided growth of single crystals using micro-structured templates [20–24]. In these methods, the precursors—mostly in soluble format—are confined to specific locations of the substrate, where they subsequently grow into patterned arrays of single crystals and polycrystalline films. Photodetector arrays fabricated using these methods, particularly those based on $MAPbBr_3$ (MA, methylammonium) single crystal perovskites [24], have shown high responsivity of 7 $A{\cdot}W^{-1}$ and specificity of 4.2×10^{11} Jones, validating their potential in image sensors. However, the inhomogeneity in the crystal growth step can lead to variations in pixel size and shape, especially when targeting micron-scale resolutions. Alternatively, inks of perovskite nanocrystals (NCs) or precursors can be inkjet- [25–28], stamp- [29], or laser-printed [30–33] into patterned single crystals or polycrystalline films. However, these printing techniques typically suffer from trade-offs between printing resolution and scalability. Electrohydrodynamic printing may hold a good balance in the resolution and scalability of perovskite patterning and enable the fabrication of multispectral photodetector arrays [34].

Complementary to the templated and printed methods, modified photolithographic methods offer a promising approach to achieving high resolution, fidelity, and scalability in perovskite patterning. However, in these cases, special photoresists [32], nondestructive developer solvents [35], or additional protection layers/dry etching steps [36] are typically required, complicating the patterning procedures. Recently, we developed a straightforward approach for direct optical patterning of perovskite NCs with ligand cross-linkers, termed as DOPPLCER [37, 38]. DOPPLCER is a resist-free photolithographic method that enables precise patterning with feature sizes below 5 μm and eliminates the need for special chemicals or processing steps mentioned above. Moreover, the patterned NC films retain their original properties, making this method particularly advantageous for high-performance device fabrication.

Here, we report the fabrication of pixelated $CsPbBr_3$ perovskite NC films through a combination of DOPPLCER patterning and post-patterning ligand exchange for efficient photodetection and imaging. Colloidal $CsPbBr_3$ NCs serve as the starting materials to create film devices. The DOPPLCER patterning process produces patterned $CsPbBr_3$ NC layers with minimal pixel sizes/linewidths of ≈ 2 μm on 2-inch wafers. Post-patterning ligand exchange partially replaces the insulating organic ligands in patterned NC layers with compact ionic ligands, significantly enhancing the charge transport properties. The patterning and ligand exchange steps can be repeated to make relatively thick NC layers (≈ 200 nm), resulting in improved light absorption and device performance. In the photoconductor configuration, the patterned NC films show almost the same responsivity (0.11 $A{\cdot}W^{-1}$ under 450 nm illumination) and detectivity (1.81×10^{11} Jones) as the non-patterned counterparts. The patterned pixelated devices, as exemplified by a 4 × 4 photodetector array, also show suppressed crosstalk between adjacent pixels and produce clearer images than the non-patterned devices. These results suggest that the combination of DOPPLCER patterning and post-patterning ligand exchange of colloidal perovskite NCs offers a promising approach for fabricating highly pixelated image sensor arrays.

2 Results and discussion

Figure 1 illustrates the patterning process of $CsPbBr_3$ NCs using DOPPLCER and the subsequent post-patterning ligand exchange for efficient photodetection and imaging. Monodisperse $CsPbBr_3$ NCs with a cubic shape and an average size of ≈ 11 nm (Fig. S1(a) in the Electronic Supplementary Material (ESM)) were synthesized using the hot injection method, as described in reported protocols [39]. These NCs are coated with a layer of hydrocarbon ligands (oleylamine and oleic acid), which were introduced during the synthesis to ensure colloidal stability. X-ray diffraction (XRD) pattern of these NCs confirms their phase purity, exhibiting an orthorhombic perovskite structure (Fig. S1(b) in the ESM). The ultraviolet–visible (UV–vis) absorption and PL spectra of NC solutions (Fig. S1(c) in the ESM) show characteristic features for $CsPbBr_3$ NCs. To fabricate pixelated devices, a stable colloidal NC solution (≈ 20 $mg{\cdot}mL^{-1}$) containing a small amount of bisazide-based cross-linkers (ethylene bis(4-azido-2,3,5,6-tetrafluoro-benzoate), the mass ratio of cross-linkers to NCs ≈ 10%, see the ESM) is spin-coated on silicon substrates with predefined readout circuits. The resulting NC film thus contains uniformly distributed cross-linkers. UV exposure (254 nm) through a photomask activates the photocross-linking reactions between ligands on adjacent NCs (Fig. 1(a)). These photochemical reactions include the photolysis of bisazides to nitrenes and the subsequent C–H insertion of nitrenes with the ligands. Detailed reaction mechanisms have been described in our previous reports [37, 40–43], and the photoactivation of cross-linkers is monitored using Fourier-transformed infrared (FTIR) spectra (Fig. S2 in the ESM). The cross-linked NCs in the exposed regions (e.g., regions with interdigitated electrodes) show drastically reduced solubility in the original solvents of NCs (e.g., toluene) compared to those in the unexposed areas. This solubility contrast allows for selective removal of unexposed NC films using these solvents as developers, resulting in patterned NC films on the electrodes. The nearly identical optical absorption and emission features of patterned and original (or termed pristine) films confirm the preservation of the optical properties of perovskite NCs throughout the patterning process (Fig. S3 in the ESM). However, the long hydrocarbon chain native ligands and organic cross-linkers, which are essential for the patterning of perovskite NCs, are insulating. These molecules hinder charge transport, which can degrade the performance of photodetectors [10]. To overcome this issue, the patterned NC films were soaked in solutions containing selected ions. This post-patterning ligand exchange process (Fig. 1(b)) replaces the native ligands and cross-linkers with compact ionic species, such as acetates and formamidinium cations (FA^+), thereby enhancing the charge transport properties. Furthermore, the DOPPLCER patterning and post-patterning ligand exchange steps can be repeated to increase the thickness of patterned devices, leading to improved device performance and capabilities in photoimaging (Fig. 1(c)), as described later.

The DOPPLCER method enables scalable patterning of perovskite NC films with high resolution and fidelity. Figures 2(a)–2(c) present the fluorescent images of patterned $CsPbBr_3$ NC films in the form of a complex logo, an array of square-shaped pixels (resembling those used in photodetectors), and lines with the width of 2 μm. The resolution of these patterns matches those defined by our photomasks. A magnified view of the patterned lines reveals a clear contrast between regions with and without NC patterns (Fig. 2(d)). This allows for the isolation of neighboring pixels, ensuring the suppression of lateral charge diffusion and the charge-sharing crosstalk, as discussed in the subsequent sections. Top-view scanning electron microscopy (SEM) images of pristine (spin-coated, without patterning procedures) and patterned films also

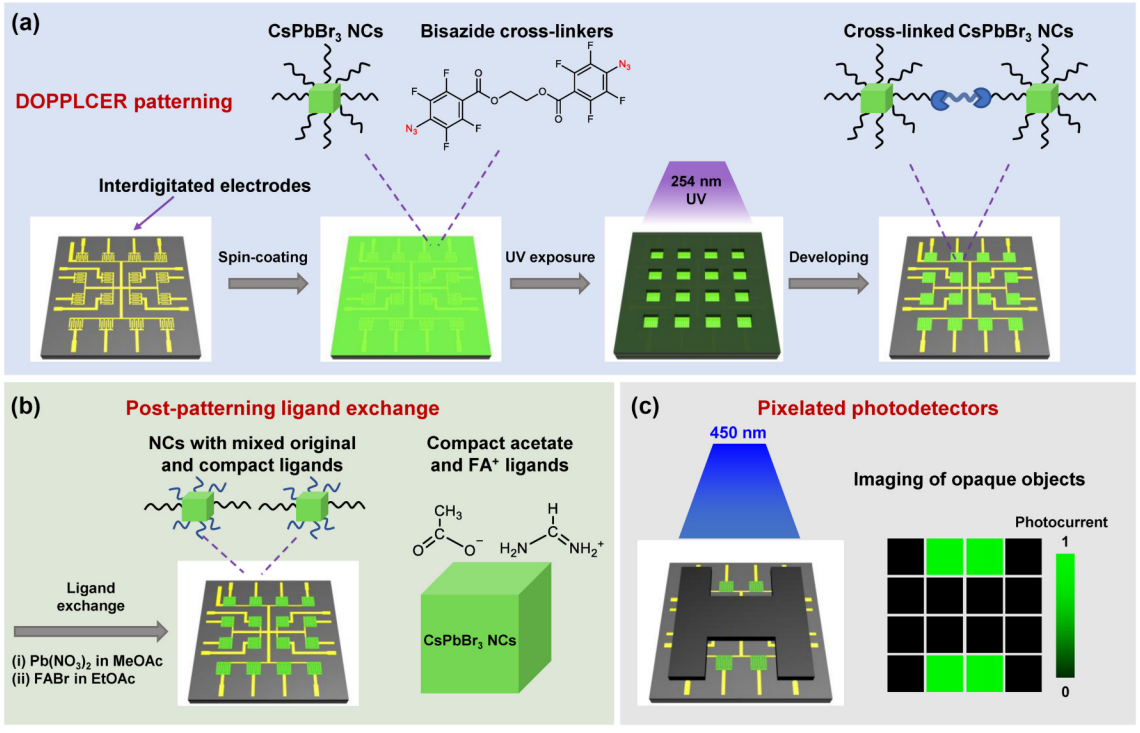

Figure 1 Patterning and post-patterning ligand exchange procedures of $CsPbBr_3$ NCs. (a) Schematic illustration of the DOPPLCER patterning procedures. A solution containing NCs and light-sensitive, bisazide-based cross-linkers is spin-coated on substrates with readout circuits (the yellow traces in (a)), exposed (e.g., 254 nm UV light) in selected regions via a photomask, and developed to form the patterned NC layers on corresponding electrodes. The patterned layer comprises cross-linked NCs. (b) Post-patterning ligand exchange processes performed to partially replace the native long-chain ligands (e.g., oleylamine, oleic acid, represented by the longer, black chains on NC surface) with compact ionic ligands (acetates and formamidinium, or FA^+, represented by the shorter, blue chains on NC surface) to enhance charge carrier transport between NCs. The ligand exchange processes include soaking the patterned NC films in a sequence of saturated $Pb(NO_3)_2$ and FABr solutions in methyl acetate (MeOAc) and ethyl acetate (EtOAc), respectively. (c) The fabricated pixelated photodetector arrays can suppress the cross-talk effect and achieve high-quality imaging of opaque objects under visible light (e.g., 450 nm), such as the "H-shaped" mask.

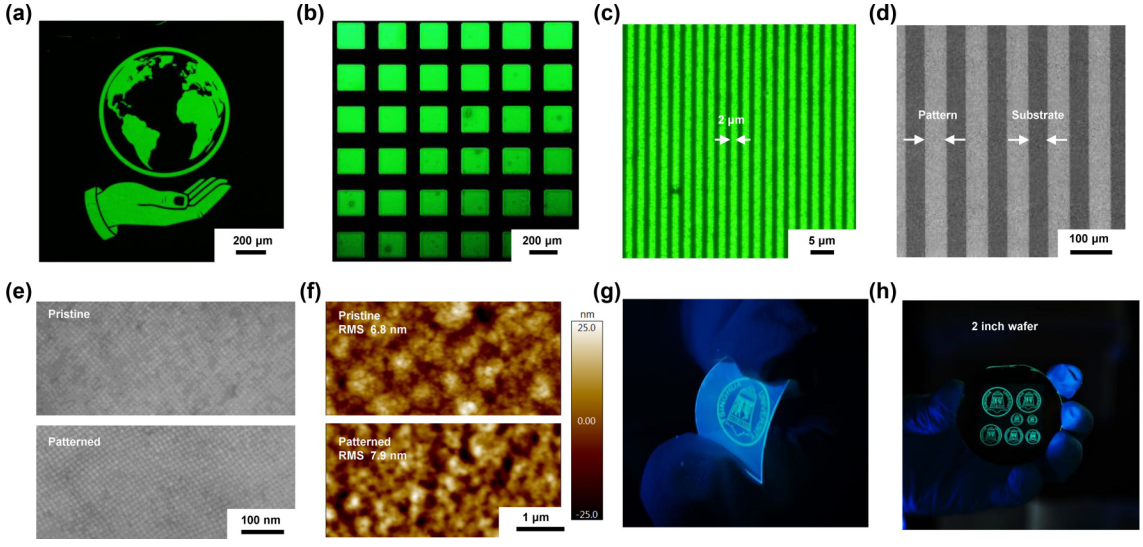

Figure 2 DOPPLCER patterning of $CsPbBr_3$ NC films. (a)–(c) Fluorescence optical microscopic images of patterned arrays of NC films in the formats of a complex logo, square pixel arrays, and line patterns with the width of 2 μm. The size of the square pixels is close to that of the interdigitated electrodes in the photodetectors. (d) SEM image of the edge of patterned lines, showing the contrast in regions containing NC films and the substrate. (e) Top-view SEM images of pristine and patterned NC films. (f) AFM images of pristine and patterned NC films (single layer by spin-coating), showing similar surface roughness. (g) and (h) Photographs of NC patterns on a flexible plastic substrate and a 2-inch wafer, respectively.

show similar morphology, featuring densely packed $CsPbBr_3$ NCs (Fig. 2(e)). Figure S4 in the ESM shows the SEM image of patterned $CsPbBr_3$ NC films in the form of an array of square-shaped pixels (resembling those used in photodetectors). Height profiles (Fig. S5 in the ESM) and atomic force microscopy (AFM) images of line patterns (Fig. 2(f)) reveal a mean square roughness (7.9 nm) comparable to that of pristine films. Moreover, the patterning is scalable, as demonstrated by its application to fabricate large-area

devices, such as those on a flexible polyethylene terephthalate substrate and a 2-inch silicon wafer, respectively (Figs. 2(g) and 2(h)). This suggests the patterning method is fully compatible with large-area substrates with predefined readout circuits, and accordingly the fabrication of devices for large-area, direct photoimaging.

We then evaluated the photoresponse behaviors of patterned $CsPbBr_3$ NC films. Figure 3(a) shows the SEM image of interdigitated Au electrode with the finger width of 10 μm. Pristine and patterned devices of $CsPbBr_3$ NC films were fabricated on these interdigitated electrodes to assess the photoresponse performance under 450 nm laser illumination in the photoconductor mode. To simplify the comparison of device performance, the patterned devices were made by exposing the entire film on the substrate during the UV cross-linking step. As a result, the patterned and pristine films had nearly identical device area and configurations, which allowed for the direct evaluation of the effect of patterning by comparing their performance. To enhance optical absorption and photocurrent, the film coating step was repeated three times for both pristine or patterned devices to increase the film thickness. Before ligand exchange, both pristine and patterned (or cross-linked) devices show linear and ohmic behaviors under applied bias, along with relatively low photocurrents (about 25 nA at 3.0 V) under illumination intensity of 13.5 $mW{\cdot}cm^{-2}$ (Fig. 3(b)). To enhance the charge transport between $CsPbBr_3$ NCs and improve the device photoconductivity, we implemented post-patterning, solid-state ligand exchange procedures as previously described [44]. These ligand exchange procedures replace both the anionic (oleate) and cationic (oleylammonium) ligands with compact ionic species. Specifically, the patterned or cross-linked NC film devices were first soaked in a saturated $Pb(NO_3)_2$ solution in methyl acetate for 30 s, followed by rinsing with methyl acetate. This process was repeated three times to induce ester hydrolysis and the generation of the acetic acids. The produced acetic acids then replace oleates from NC surface. It is noteworthy that the nitrates from $Pb(NO_3)_2$ were not incorporated into the NC films, according to previous work by Luther and co-workers [44]. The addition of $Pb(NO_3)_2$ may influence the amount of adventitious water (in the glovebox) involved in the ester hydrolysis [44]. Subsequently, NC films were soaked in a saturated FABr (formamidinium bromide) solution in ethyl acetate for 90 s, during which the FA^+ replace the oleylammonium ligands [44]. The oleylammonium–to–formamidinium ligand exchange process was validated by FTIR analysis (Fig. 3(c)). After FABr treatment, NC films show characteristic peaks at ≈ 1720 and 3348 cm^{-1}, corresponding to ν(C=N) and ν(C=N–H_2^+) vibrations from the FA^+ ligands. Notably, the intensity of C–H stretching peaks significantly decreased but still persisted in the FTIR spectra of both pristine and patterned/cross-linked NC films, suggesting that the ligand exchange was partial, which is consistent with those observed in previous reports [44–46]. The patterned films, both before and after ligand exchange, show peaks at around 1300 cm^{-1}, which correspond to asymmetric stretching of C–N–C bonds due to cross-linking reaction during patterning. We compared the optical absorption spectra of cross-linked NC films before and after ligand exchange and observed no notable changes in the peak positions (Fig. S6(a) in the ESM). However, the PL intensities of NC films or patterns (Figs. S6(b) and S7 in the ESM) decreased after ligand exchange, which is due to the removal of the long hydrocarbon ligands. Additionally, we analyzed the morphology of the patterned/cross-linked NC films before and after ligand exchange (Figs. S7 and S8 in the ESM). The resolution and morphology of the patterned lines also remain nearly unchanged before and after ligand exchange. The relatively high surface roughness of ligand-exchanged NC films (Fig. S8 in the ESM) was probably due to the repeated soaking and rinsing processes during ligand exchange and successive coating of three layers of NCs. Collectively, these results suggest that the post-patterning ligand exchange process can partially replace the long, insulating ligands, while preserving the structural integrity of the NC patterns. Additionally, the patterning and ligand exchange process can be applied to perovskite NCs of other compositions, such as $CsPbI_xBr_{3-x}$ (Fig. S9 in the ESM).

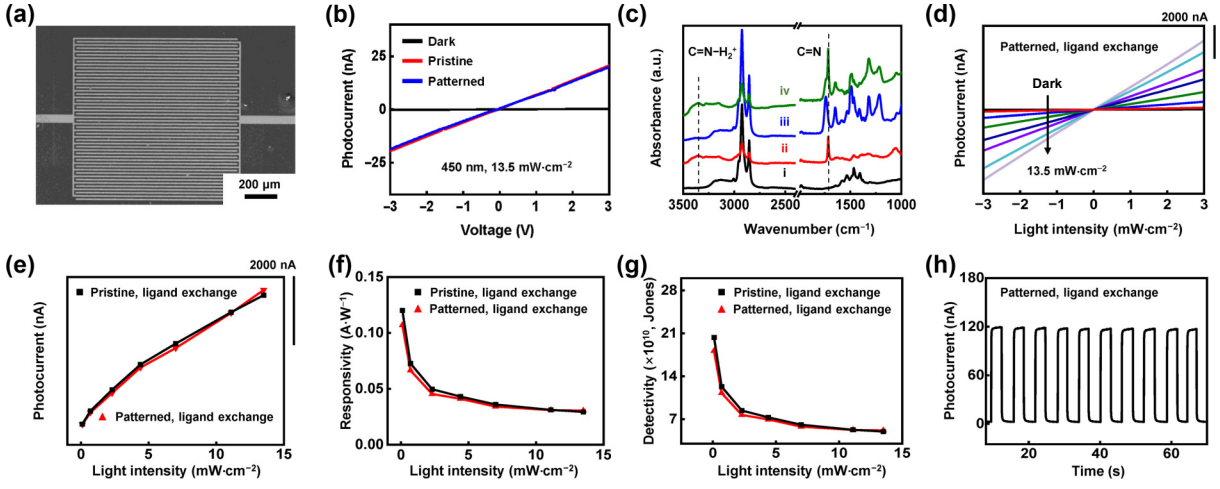

Figure 3 Photoresponse behavior of patterned $CsPbBr_3$ NC film-based photoconductive devices after ligand exchange. (a) SEM image of the Au interdigital electrode. (b) *I*–*V* curves of pristine and patterned devices without ligand exchange. Photocurrents were measured under 450 nm light illumination (light intensity, 13.5 $mW{\cdot}cm^{-2}$). Dark current was also measured for comparison. (c) FTIR of pristine ((i), before; (ii), after) and patterned devices (iii, before; iv, after) before and after ligand exchange. After ligand exchange, the spectra show vibrational peaks corresponding to *ν*(C=N) and *ν*(C=N–H_2^+) from the FA^+ ligands. (d) *I*–*V* curves of patterned device after post-patterning ligand exchange taken under 450 nm light illumination. Light intensities varied from 0.1 to 13.5 $mW{\cdot}cm^{-2}$ (dark, 0.1, 0.7, 2.3, 4.4, 7.0, 11.1, and 13.5 $mW{\cdot}cm^{-2}$). (e) Photocurrent–light intensity curves of pristine and patterned devices after ligand exchange. Bias, 3.0 V. (f) and (g) Responsivity and detectivity of pristine and patterned devices after ligand exchange under 450 nm light illumination and a bias of 3.0 V. (h) On–off performance of patterned devices after ligand exchange under light illumination at 0.1 $mW{\cdot}cm^{-2}$ and a bias of 3.0 V.

The post-patterning ligand exchange process significantly enhances the photoconductivity of the devices. The photocurrent of pristine NC devices increased from ≈ 25 nA to ≈ 3.9 μA at a bias of 3.0 V under 450 nm laser illumination (13.5 mW·cm^{-2}), as shown in Fig. S10(a) in the ESM. Similarly, the patterned/cross-linked devices, after ligand exchange, showed a comparable photocurrent of about 4.1 μA under the same illumination and bias conditions (Fig. 3(d)), with a similar trend observed in the photocurrent–light intensity relation (Fig. 3(e)). The calculated responsivity (0.12 and 0.11 A·W^{-1}) and detectivity (2.04 × 10^{11} and 1.81 × 10^{11} Jones) for pristine and patterned devices, after ligand exchange, were also almost identical, as shown in Figs. 3(f) and 3(g). The only difference was the longer soaking time required for ligand exchange in the patterned devices, likely due to the presence of cross-linked ligands. Figure 3(h) and Fig. S10(b) in the ESM show the stable operation of the patterned devices under alternating on–off cycles, with fast response times. The rise and decay times for patterned devices were estimated to be 46 and 22 ms (Fig. S11 in the ESM), respectively, which are comparable to those reported for perovskite NC based photodetectors in previous literatures (see Table S1 in the ESM). These comparisons indicate that the integration of DOPPLCER patterning and post-patterning ligand exchange processes enables the fabrication of pixelated devices with decent photoconductivity.

The pixelation of $CsPbBr_3$ NC layers atop predefined interdigitated electrodes is crucial for minimizing crosstalk caused by lateral charge diffusion or charge sharing and for achieving high imaging resolution, as illustrated in Figs. 4(a) and 4(b). In pristine devices without pixelation, measurable light currents can still be detected from unexposed regions due to the charge diffusion from adjacent irradiated parts. In contrast, the isolation of pixels in patterned devices prevents such charge diffusion, resulting in improved imaging contrast. To demonstrate this, we fabricated proof-of-concept image sensors on readout circuits with 4 × 4 interdigitated electrodes, where the active layers comprised either pristine or patterned (with patterns matching the 4 × 4 electrode arrays, Fig. S12 in the ESM) perovskite NCs. In both cases, ligand exchange was performed on the pristine or patterned devices to enhance photoconductivity. When the entire device was exposed to a 450 nm light source, photocurrents corresponding to the 16 electrodes/pixels were sequentially measured, normalized (denoted as I_{norm}), and converted as an image. Figures 4(c) and 4(d) show the spatial distribution of photocurrents. The coefficient of variation, or the relative standard deviation, of photocurrents for pixels in pristine and patterned devices were 12.9% and 16.8%, respectively. This indicates that the two types of devices show similar uniformity in the performance of each pixel, despite that the measured photocurrents in the pixels of non-patterned devices contain contributions from their neighbors. The suppression of crosstalk in patterned devices can be demonstrated in the imaging tests with opaque, polyimide-based masks (about 100 μm in thickness) of different shapes (e.g., "II-shaped" in Figs. 4(e) and 4(f)). The "II-shaped" masks selectively block 450 nm light for certain pixels in the detectors (i.e., those in the dashed boxes in Figs. 4(e) and 4(f)), creating an image reflecting the photocurrent contrast in irradiated and blocked regions. The patterned devices show much higher contrast in the photocurrents of the irradiated and blocked regions, producing a clear "II" shape image (Fig. 4(f)). In contrast, some of the blocked pixels in the pristine or non-patterned devices exhibit small photocurrents, likely due to leaking currents from the adjacent, irradiated pixels. We also performed the imaging tests with masks in the shapes of letters "T", "H", and "U". The resulting images clearly and accurately displayed the shapes of the masks, showcasing the potential of patterned perovskite NC devices for high-resolution photoimaging (Figs. 4(g)–4(i)).

3 Conclusions

In summary, we demonstrated the use of DOPPLCER patterning and post-patterning ligand exchange processes to fabricate pixelated $CsPbBr_3$ NC devices for photodetection. This two-step approach, yields NC patterns with high resolution (pixel/line size of 2 μm), fidelity, and scalability. After ligand exchange, the responsivity and detectivity of the patterned detectors match those of non-patterned devices and are on par with those reported for perovskite NC based

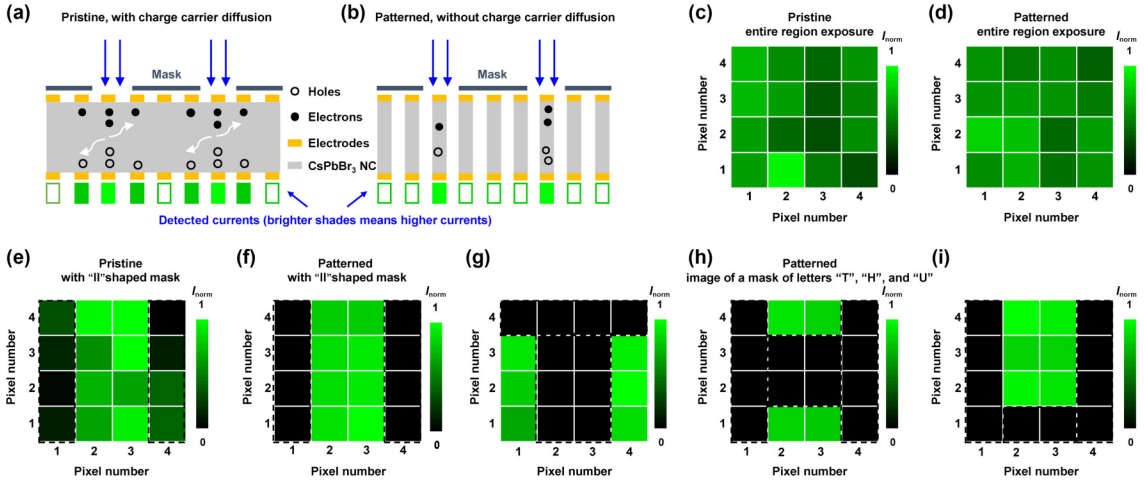

Figure 4 Imaging tests with pixelated photodetector arrays made from patterned and ligand-exchanged $CsPbBr_3$ NC films. (a) and (b) Schematic diagram of the charge-sharing effect in pristine (non-patterned) and patterned devices. In the former, the photogenerated carriers in the exposed regions can spread to the adjacent regions, producing currents in the neighboring, unexposed pixels and compromised imaging quality. By contrast, the isolation of pixels in the latter case eliminates this effect and only the exposed regions show photocurrents. (c) and (d) Photocurrent distribution in the pristine and patterned devices, both containing a 4 × 4 array of electrodes, when the entire device is exposed to 450 nm light source. (e) and (f) Photocurrent distribution in the pristine and patterned detector arrays in the case of imaging with the "II-shaped" opaque polyimide mask. The black dashed boxes indicate the area blocked by the mask. (g)–(i) Imaging with patterned detector arrays to show the image of letters "T", "H", and "U" by using opaque polyimide masks. The black dashed boxes indicate the blocked regions.

photodetectors. Importantly, the patterned pixelated devices exhibit reduced charge-sharing crosstalk and improved imaging clarity and sharper contours. We note that various ligand exchange and thermal treatment strategies have been developed to improve the NC coupling and increase the performance of perovskite NC devices [47–50]. We expect that the combination of DOPPLCER and these post-patterning ligand exchange offers an alternative approach to constructing high-resolution and efficient photodetectors based on perovskites for image sensing applications.

Electronic Supplementary Material: Supplementary material (supplementary texts on materials, synthesis of $CsPbBr_3$ NCs, DOPPLCER patterning process, post-patterning ligand exchange process, fabrication and characterization procedures of photoconductors, material characterization techniques, supplementary figures on characterizations of $CsPbBr_3$ NCs, FTIR spectra of $CsPbBr_3$ NC films with or without cross-linkers, optical absorption and emission spectra of pristine and patterned $CsPbBr_3$ NC films, SEM image and height profiles of patterned NC films, optical and emission spectra, and optical, SEM, and AFM images of patterned NC films before and after ligand exchange, optical images and FTIR spectra of patterned $CsPbI_xBr_{3-x}$ films before and after ligand exchange, *I*–*V* curves of pristine devices after ligand exchange, rise and decay times of patterned devices, fluorescence optical microscopic and SEM images and performance of patterned photodetector arrays after ligand exchange) is available in the online version of this article at https://doi.org/10.26599/NR.2025.94907279.

Data availability

All data needed to support the conclusions in the paper are presented in the manuscript and the Electronic Supplementary Material.

Acknowledgements

This work was financially supported by the National Natural Science Foundation of China (No. 22274087) (H. Z.), Tsinghua University Dushi Program (H. Z.), and the National Key Research and Development Program of China (No. 2022YFB3204100) (T.-L. R.).

Declaration of competing interest

All the contributing authors report no conflict of interests in this work.

Author contribution statement

H. A., G.-H. D., and H. Z. led in designing the experiment. H. A. and G.-H. D. led in performing the experiments and analyzing the data with help from H. W. Q., D. L., F. L., J. Y. H., W. Y. L., and M. F. C. H. Z., H. A., and G.-H. D. co-wrote the original manuscript. T.-L. R., H. Z., and J. H. L. supervised the project, acquired funding, and provided resources for this research. All the authors have approved the final manuscript.

Use of AI statement

None.

References

[1] Jena, A. K.; Kulkarni, A.; Miyasaka, T. Halide perovskite photovoltaics: Background, status, and future prospects. *Chem. Rev.* **2019**, *119*, 3036–3103.
[2] Lin, K. B.; Xing, J.; Quan, L. N.; de Arquer, F. P. G.; Gong, X. W.; Lu, J. X.; Xie, L. Q.; Zhao, W. J.; Zhang, D.; Yan, C. Z. et al. Perovskite light-emitting diodes with external quantum efficiency exceeding 20 per cent. *Nature* **2018**, *562*, 245–248.
[3] García de Arquer, F. P.; Armin, A.; Meredith, P.; Sargent, E. H. Solution-processed semiconductors for next-generation photodetectors. *Nat. Rev. Mater.* **2017**, *2*, 16100.
[4] Wang, H.; Kim, D. H. Perovskite-based photodetectors: Materials and devices. *Chem. Soc. Rev.* **2017**, *46*, 5204–5236.
[5] Tang, Y. J.; Jin, P.; Wang, Y.; Li, D. W.; Chen, Y. T.; Ran, P.; Fan, W.; Liang, K.; Ren, H. H.; Xu, X. H. et al. Enabling low-drift flexible perovskite photodetectors by electrical modulation for wearable health monitoring and weak light imaging. *Nat. Commun.* **2023**, *14*, 4961.
[6] Min, L. L.; Sun, H. X.; Guo, L. Q.; Wang, M.; Cao, F. R.; Zhong, J.; Li, L. Frequency-selective perovskite photodetector for anti-interference optical communications. *Nat. Commun.* **2024**, *15*, 2066.
[7] Wu, W. T.; Li, L. L.; Li, Z. X.; Sun, J. Z.; Wang, L. L. Extensible integrated system for real-time monitoring of cardiovascular physiological signals and limb health. *Adv. Mater.* **2023**, *35*, 2304596.
[8] Adinolfi, V.; Ouellette, O.; Saidaminov, M. I.; Walters, G.; Abdelhady, A. L.; Bakr, O. M.; Sargent, E. H. Fast and sensitive solution-processed visible-blind perovskite UV photodetectors. *Adv. Mater.* **2016**, *28*, 7264–7268.
[9] Dou, L. T.; Yang, Y.; You, J. B.; Hong, Z. R.; Chang, W. H.; Li, G.; Yang, Y. Solution-processed hybrid perovskite photodetectors with high detectivity. *Nat. Commun.* **2014**, *5*, 5404.
[10] Bi, C. H.; Kershaw, S. V.; Rogach, A. L.; Tian, J. J. Improved stability and photodetector performance of $CsPbI_3$ perovskite quantum dots by ligand exchange with aminoethanethiol. *Adv. Funct. Mater.* **2019**, *29*, 1902446.
[11] Wang, Y.; Song, L.; Chen, Y.; Huang, W. Emerging new-generation photodetectors based on low-dimensional halide perovskites. *ACS Photonics* **2020**, *7*, 10–28.
[12] Wangyang, P. H.; Gong, C. H.; Rao, G. F.; Hu, K.; Wang, X. P.; Yan, C. Y.; Dai, L. P.; Wu, C. Y.; Xiong, J. Recent advances in halide perovskite photodetectors based on different dimensional materials. *Adv. Opt. Mater.* **2018**, *6*, 1701302.
[13] Yang, X.; Wu, J.; Liu, T.; Zhu, R. Patterned perovskites for optoelectronic applications. *Small Methods* **2018**, *2*, 1800110.
[14] Jeong, B.; Han, H.; Park, C. Micro- and nanopatterning of halide perovskites where crystal engineering for emerging photoelectronics meets integrated device array technology. *Adv. Mater.* **2020**, *32*, 2000597.
[15] Wang, G. M.; Li, D. H.; Cheng, H. C.; Li, Y. J.; Chen, C. Y.; Yin, A. X.; Zhao, Z. P.; Lin, Z. Y.; Wu, H.; He, Q. et al. Wafer-scale growth of large arrays of perovskite microplate crystals for functional electronics and optoelectronics. *Sci. Adv.* **2015**, *1*, e1500613.
[16] Lee, W.; Lee, J.; Yun, H.; Kim, J.; Park, J.; Choi, C.; Kim, D. C.; Seo, H.; Lee, H.; Yu, J. W. et al. High-resolution spin-on-patterning of perovskite thin films for a multiplexed image sensor array. *Adv. Mater.* **2017**, *29*, 1702902.
[17] Wu, W. Q.; Wang, X. D.; Han, X.; Yang, Z.; Gao, G. Y.; Zhang, Y. F.; Hu, J. F.; Tan, Y. W.; Pan, A. L.; Pan, C. F. Flexible photodetector arrays based on patterned $CH_3NH_3PbI_{3-x}Cl_x$ perovskite film for real-time photosensing and imaging. *Adv. Mater.* **2019**, *31*, 1805913.
[18] Lin, C. K.; Zhao, Q. C.; Zhang, Y.; Cestellos-Blanco, S.; Kong, Q.; Lai, M. L.; Kang, J.; Yang, P. D. Two-step patterning of scalable all-inorganic halide perovskite arrays. *ACS Nano* **2020**, *14*, 3500–3508.
[19] Xu, Z. S.; Pan, X. J.; Lu, H.; Lu, Q. C.; Liang, Y. G.; He, Z. P.; Zhu, Y. Z.; Yu, Y.; Wu, W. Q.; Han, X. et al. Surface energy-assisted patterning of vapor deposited all-inorganic perovskite arrays for wearable optoelectronics. *Adv. Sci.* **2024**, *11*, 2402635.
[20] Gao, H. F.; Feng, J. G.; Pi, Y. Y.; Zhou, Z. H.; Zhang, B.; Wu, Y. C.;

Wang, X. D.; Jiang, X. Y.; Jiang, L. Bandgap engineering of single-crystalline perovskite arrays for high-performance photodetectors. *Adv. Funct. Mater.* **2018**, *28*, 1804349.

[21] Zhao, J. J.; Li, H. H.; Qiu, Y. C.; Feng, J. G.; Yang, J. C.; He, K.; Wu, P. H.; Wang, N. Z.; Gao, H. F.; Jiang, L. et al. Programmable single-crystalline PbI_2 microplate arrays and their organic/inorganic heterojunctions. *Adv. Funct. Mater.* **2020**, *30*, 2003631.

[22] Yu, X. Y.; Wu, L. Z.; Yang, D.; Cao, M. H.; Fan, X.; Lin, H. P.; Zhong, Q. X.; Xu, Y.; Zhang, Q. Hydrochromic $CsPbBr_3$ nanocrystals for anti-counterfeiting. *Angew. Chem., Int. Ed.* **2020**, *59*, 14527–14532.

[23] Zhang, J. L.; Yang, Y. F.; Li, W. J.; Tang, Z. G.; Hu, Z. Y.; Wei, H. T.; Zhang, J. H.; Yang, B. Precise arraying of perovskite single crystals through droplet-assisted self-alignment. *Sci. Adv.* **2024**, *10*, eado0873.

[24] Xu, Z. S.; Han, X.; Wu, W. Q.; Li, F. T.; Wang, R.; Lu, H.; Lu, Q. C.; Ge, B. H.; Cheng, N. Y.; Li, X. Y. et al. Controlled on-chip fabrication of large-scale perovskite single crystal arrays for high-performance laser and photodetector integration. *Light Sci. Appl.* **2023**, *12*, 67.

[25] Wei, C. T.; Su, W. M.; Li, J. T.; Xu, B.; Shan, Q. S.; Wu, Y.; Zhang, F. J.; Luo, M. M.; Xiang, H. Y.; Cui, Z. et al. A universal ternary-solvent-ink strategy toward efficient inkjet-printed perovskite quantum dot light-emitting diodes. *Adv. Mater.* **2022**, *34*, 2107798.

[26] Shi, L. F.; Meng, L. H.; Jiang, F.; Ge, Y.; Li, F.; Wu, X. G.; Zhong, H. Z. *In situ* inkjet printing strategy for fabricating perovskite quantum dot patterns. *Adv. Funct. Mater.* **2019**, *29*, 1903648.

[27] Gu, Z. K.; Wang, K.; Li, H. Z.; Gao, M.; Li, L. H.; Kuang, M. X.; Zhao, Y. S.; Li, M. Z.; Song, Y. L. Direct-writing multifunctional perovskite single crystal arrays by inkjet printing. *Small* **2017**, *13*, 1603217.

[28] Zhu, M. H.; Duan, Y. Q.; Liu, N.; Li, H. G.; Li, J. H.; Du, P. P.; Tan, Z. F.; Niu, G. D.; Gao, L.; Huang, Y. A. et al. Electrohydrodynamically printed high-resolution full-color hybrid perovskites. *Adv. Funct. Mater.* **2019**, *29*, 1903294.

[29] Du, J. S.; Shin, D.; Stanev, T. K.; Musumeci, C.; Xie, Z.; Huang, Z. Y.; Lai, M. L.; Sun, L.; Zhou, W. J.; Stern, N. P. et al. Halide perovskite nanocrystal arrays: Multiplexed synthesis and size-dependent emission. *Sci. Adv.* **2020**, *6*, eabc4959.

[30] Liang, S. Y.; Liu, Y. F.; Zhang, H. J.; Ji, Z. K.; Xia, H. High-quality patterning of $CsPbBr_3$ perovskite films through lamination-assisted femtosecond laser ablation toward light-emitting diodes. *ACS Appl. Mater. Interfaces* **2022**, *14*, 46958–46963.

[31] Zhan, W. J.; Meng, L. H.; Shao, C. D.; Wu, X. G.; Shi, K. B.; Zhong, H. Z. *In situ* patterning perovskite quantum dots by direct laser writing fabrication. *ACS Photonics* **2021**, *8*, 765–770.

[32] Lin, C. H.; Zeng, Q. J.; Lafalce, E.; Yu, S. T.; Smith, M. J.; Yoon, Y. J.; Chang, Y. J.; Jiang, Y.; Lin, Z. Q.; Vardeny, Z. V. et al. Large-area lasing and multicolor perovskite quantum dot patterns. *Adv. Opt. Mater.* **2018**, *6*, 1800474.

[33] Chen, X. G.; Lin, L. H.; Huang, G. Y.; Chen, X. M.; Li, X. Z.; Zhou, Y. K.; Zou, Y. X.; Fu, T. R.; Li, P.; Li, Z. C. et al. Optofluidic crystallithography for directed growth of single-crystalline halide perovskites. *Nat. Commun.* **2024**, *15*, 3677.

[34] Duan, Y. Q.; Yu, R.; Zhang, H. Y.; Yang, W. L.; Xie, W. S.; Huang, Y. A.; Yin, Z. P. Programmable, high-resolution printing of spatially graded perovskites for multispectral photodetectors. *Adv. Mater.* **2024**, *36*, 2313946.

[35] Dun, G. H.; Zhang, H. N.; Qin, K.; Tan, X. C.; Zhao, R.; Chen, M.; Huang, Y.; Geng, X. S.; Li, Y. Y.; Li, Y. H. et al. Wafer-scale photolithography-pixeled Pb-free perovskite X-ray detectors. *ACS Nano* **2022**, *16*, 10199–10208.

[36] Zou, C.; Chang, C.; Sun, D.; Böhringer, K. F.; Lin, L. Y. Photolithographic patterning of perovskite thin films for multicolor display applications. *Nano Lett.* **2020**, *20*, 3710–3717.

[37] Liu, D.; Weng, K. K.; Lu, S. Y.; Li, F.; Abudukeremu, H.; Zhang, L. P.; Yang, Y. C.; Hou, J. Y.; Qiu, H. W.; Fu, Z. et al. Direct optical patterning of perovskite nanocrystals with ligand cross-linkers. *Sci. Adv.* **2022**, *8*, eabm8433.

[38] Liu, D.; Weng, K. K.; Zhao, H. F.; Wang, S.; Qiu, H. W.; Luo, X. Y.; Lu, S. Y.; Duan, L.; Bai, S.; Zhang, H. et al. Nondestructive direct optical patterning of perovskite nanocrystals with carbene-based ligand cross-linkers. *ACS Nano* **2024**, *18*, 6896–6907.

[39] Protesescu, L.; Yakunin, S.; Bodnarchuk, M. I.; Krieg, F.; Caputo, R.; Hendon, C. H.; Yang, R. X.; Walsh, A.; Kovalenko, M. V. Nanocrystals of cesium lead halide perovskites ($CsPbX_3$, X = Cl, Br, and I): Novel optoelectronic materials showing bright emission with wide color gamut. *Nano Lett.* **2015**, *15*, 3692–3696.

[40] Lu, S. Y.; Fu, Z.; Li, F.; Weng, K. K.; Zhou, L. K.; Zhang, L. P.; Yang, Y. C.; Qiu, H. W.; Liu, D.; Qing, W. Y. et al. Beyond a linker: The role of photochemistry of crosslinkers in the direct optical patterning of colloidal nanocrystals. *Angew. Chem., Int. Ed.* **2022**, *61*, e202202633.

[41] Li, F.; Chen, C. H.; Lu, S. Y.; Chen, X. G.; Liu, W. Y.; Weng, K. K.; Fu, Z.; Liu, D.; Zhang, L. P.; Abudukeremu, H. et al. Direct patterning of colloidal nanocrystals via thermally activated ligand chemistry. *ACS Nano* **2022**, *16*, 13674–13683.

[42] Wang, S.; Lu, S. Y.; Tian, X. L.; Liu, W. Y.; Si, Y. L.; Yang, Y. C.; Qiu, H. W.; Zhang, H.; Li, J. H. A general approach to stabilize nanocrystal superlattices by covalently bonded ligands. *ACS Nano* **2023**, *17*, 2792–2801.

[43] Qing, W. Y.; Si, Y. L.; Cai, M. F.; Zhou, L. K.; Wu, L. J.; Hou, Z. W.; Liu, D.; Tian, X. L.; Liu, W. Y.; Lin, L. H. et al. Photosensitizer-assisted direct 2D patterning and 3D printing of colloidal quantum dots. *Nano Res.* **2024**, *17*, 10460–10466.

[44] Wheeler, L. M.; Sanehira, E. M.; Marshall, A. R.; Schulz, P.; Suri, M.;Anderson, N. C.; Christians, J. A.; Nordlund, D.; Sokaras, D.; Kroll, T. et al. Targeted ligand-exchange chemistry on cesium lead halide perovskite quantum dots for high-efficiency photovoltaics. *J. Am. Chem. Soc.* **2018**, *140*, 10504–10513.

[45] Swarnkar, A.; Marshall, A. R.; Sanehira, E. M.; Chernomordik, B. D.; Moore, D. T.; Christians, J. A.; Chakrabarti, T.; Luther, J. M. Quantum dot-induced phase stabilization of α-$CsPbI_3$ perovskite for high-efficiency photovoltaics. *Science* **2016**, *354*, 92–95.

[46] Kim, J.; Koo, B.; Kim, W. H.; Choi, J.; Choi, C.; Lim, S. J.; Lee, J. S.; Kim, D. H.; Ko, M. J.; Kim, Y. Alkali acetate-assisted enhanced electronic coupling in $CsPbI_3$ perovskite quantum dot solids for improved photovoltaics. *Nano Energy* **2019**, *66*, 104130.

[47] Fiuza-Maneiro, N.; Sun, K.; López-Fernández, I.; Gómez-Graña, S.; Müller-Buschbaum, P.; Polavarapu, L. Ligand chemistry of inorganic lead halide perovskite nanocrystals. *ACS Energy Lett.* **2023**, *8*, 1152–1191.

[48] Aqoma, H.; Lee, S. H.; Imran, I. F.; Hwang, J. H.; Lee, S. H.; Jang, S. Y. Alkyl ammonium iodide-based ligand exchange strategy for high-efficiency organic-cation perovskite quantum dot solar cells. *Nat. Energy* **2024**, *9*, 324–332.

[49] Jia, D. L.; Chen, J. X.; Yu, M.; Liu, J. H.; Johansson, E. M. J.; Hagfeldt, A.; Zhang, X. L. Dual passivation of $CsPbI_3$ perovskite nanocrystals with amino acid ligands for efficient quantum dot solar cells. *Small* **2020**, *16*, 2001772.

[50] Xue, J. J.; Lee, J. W.; Dai, Z. H.; Wang, R.; Nuryyeva, S.; Liao, M. E.; Chang, S. Y.; Meng, L.; Meng, D.; Sun, P. Y. et al. Surface ligand management for stable $FAPbI_3$ perovskite quantum dot solar cells. *Joule* **2018**, *2*, 1866–1878.